Continuous turbulent liquid-liquid emulsification using open-cell solid foams: experimental investigation and modelling

Noureddine Lebaz, Kristy Touma, Yousra Guedda, Régis Philippe, Nida Sheibat-Othman

Continuous turbulent liquid-liquid emulsification using open-cell solid foams: experimental investigation and modelling

Noureddine Lebaz[1*]; Kristy Touma[1]; Yousra Guedda[1]; Régis Philippe[2]; Nida Sheibat-Othman[1]

[1] Universite Claude Bernard Lyon 1, LAGEPP UMR 5007 CNRS, F-69100, Villeurbanne, France

[2] Catalyse Polymérisation Procédés & Matériaux (CP2M), Université Lyon, UMR 5128 CNRS – CPE Lyon – UCBL, 43 boulevard du 11 novembre 1918, F-69100 Villeurbanne, France

Abstract

The study investigates the efficiency of liquid-liquid emulsification using three types of open-cell solid foams. Initially, the pressure drop profiles revealed the non-negligible impact of the inertial term at a low viscosity of the continuous phase, with profiles becoming more linear at higher viscosities. The Darcy-Forchheimer model effectively predicted pressure drops with a maximum mean relative error of 14 %. Emulsification performance (seen as a decrease in the droplet size) was then evaluated by varying dispersed phase viscosity, superficial fluid flow velocity and foam insert packing length, comparing results with structured static mixers (SMX+). The droplet size of the dispersed phase rapidly decreased within the first foam inserts before stabilizing at a length of 175 mm. Under the same superficial velocity, the mean droplet diameter is correlated to the foam's mean pore size. SMX+ mixers exhibited emulsification capability comparable to solid foam with the largest pores, while medium and small pore foams produced smaller droplets. Finally, the Middleman's correlation with viscosity correction accurately predicted mean droplet size at equilibrium and across various scenarios.

[*] Corresponding author. Address : LAGEPP, Université Claude Bernard Lyon 1, bât 308G ESCPE-Lyon, 43 bd du 11 Novembre 1918, Villeurbanne 69622 France. Tel.: +33 04 72 43 18 55; Fax: +33 04 72 43 16 99
Email address: noureddine.lebaz@univ-lyon1.fr (Noureddine Lebaz)

Keywords: open-cell solid foams; emulsification; pressure drops; droplet size distribution; energy dissipation

1 Introduction

Open-cell solid foam (OCSF) packings are considered as intensified alternatives to classical dense packed beds in many fields such as catalysis [1,2], distillation [3], energy systems [4,5], and multiphase reactors [6–8]. They represent an interconnected random network of solid struts, offering a high specific surface area and high permeability, so promoting mass and heat transfer with reduced pressure drop [9,10]. Intensive research has been carried out over the last two decades to develop novel manufacturing techniques as well as characterisation and performance assessment of open-cell solid foams [11].

Emulsions are liquid-liquid dispersions of at least two non-miscible fluids in the form of droplets (dispersed phase) suspended in the continuous phase and stabilised with surfactants [12]. The emulsion properties such as its flowability, rheology and texture are ultimately linked with the droplet size distribution (DSD). Energy input is required to ensure efficient mixing and droplet breakage to attain the desired DSD. This is usually achieved using classical stirred tanks, rotor-stator devices and membranes [13]. At the industrial scale, seeking a continuous emulsification process is highly desired to increase productivity.

Structured static mixers with different geometrical characteristics are known to be efficient for liquid-liquid dispersion, besides many other applications [14]. Unlike OCSFs which have local random pore size and orientation, the classical static mixers have structured configurations in the form of crossed solid bars or grids. Such structure allows dividing and redistributing the flow streamlines to promote chaotic mixing of the fluids [15]. Static mixers are directly inserted in pipes and channels, by arranging identical elements in series. They offer a spatially uniform energy dissipation rate allowing the emulsification of highly viscous fluids [16,17]. However, because of their ordered structure, their manufacturing suffers from difficulties related to technical constraints such as respecting the porosity set-point and the structure of the element, which should in turn respect some criteria to guarantee the mechanical integrity of the system [18]. At the process scale, this usually results in high-pressure drops, so continuous efforts are made to propose new geometries with enhanced mixing efficiency and reduced pressure drop [19,20].

Because of the ease in their manufacturing and their random structure, OCSFs overcome the limitations of the classical static mixers in terms of the correlation between void fraction and

pore size, with the pressure drop and mechanical properties. They offer a specific surface area of up to 7 000 m^2 m^{-3}, a void fraction between 75 % and 95 %, and pores of size less than a millimetre, while keeping interesting mechanical properties [21–23]. Despite these interesting features, only few studies are found in the literature regarding the use of OCSFs as emulsification support. Wang et al. (2022) studied a liquid-liquid emulsification process in a rotating solid foam stirrer tank [24]. The traditional stirring paddles were substituted by a porous packing, with potential catalysts deposition, and were tested in different applications involving gas-liquid and solid-liquid mass transfer, such as wastewater treatment by ozone [25] and the catalytic oxidation of glucose [26]. A kerosene-water system was considered and the effect of varying the rotational speed, the dispersed phase volume fraction, the continuous phase viscosity and the packing length on the Sauter mean diameter (d_{32}) and the DSD were investigated. The solid foam stirrer was made of Al_2O_3 hydrophobic material with a porosity of 0.88 and an average pore size of 0.9 mm (so a pore density, i.e. pores per inch (PPI), of 20). The system showed a superior emulsification performance compared to a classical Rushton turbine with the same energy input. However, bimodal droplet distributions were obtained especially in the case of high continuous phase viscosity which is explained by the non-homogeneous distribution of the energy dissipation rate in the system [27]. Luo et al. (2017) investigated cyclohexane dispersion in water using a helical tube reactor [22]. The emulsification system comprised a straight tube packed with nickel foam elements followed by a helical tube. Three nickel foams were tested having the same porosity (0.96) and different mean pore diameters (1.27 mm, 0.85 mm and 0.64 mm). It was shown that the d_{32} of the emulsions was directly correlated to the mean pore size of the nickel foams, and no evolution in the drop size was observed after 4 packing elements (of 18 mm length each). Moreover, the energy dissipation was dependent on the pre-dispersion unit, since the d_{32} was the same at the inlet and the outlet of the helical tube independently of the fluid flow rate and the curvature of the helical tube. More recently, Hapanowicz et al. (2023) studied the liquid-liquid dispersion (oil-in-water and water-in-oil) in a horizontal tube packed with aluminium and nickel foams having almost the same structural properties [28]. However, only pressure drops were reported without any information on the quality of the dispersion in terms of the DSD or mean droplet diameter.

This study aims to investigate the continuous liquid-liquid emulsification capabilities of three OCSFs having various geometrical properties under different conditions including the type of foam (i.e. porosity, pore size), the total length of the packing zone, the fluid flow rate and the

viscosity of the continuous and dispersed phases. The results are compared to those obtained with a reference commercial structured static mixer in terms of pressure drop and DSD under the same conditions. Finally, different correlations are tested for the prediction of the mean droplet size at equilibrium.

2 Materials and methods

2.1 Materials

The single direct O/W emulsions were prepared using ultrapure water (Synergy unit system, Millipore, France) and silicone oils (Sigma-Aldrich, Germany) of different viscosities. Polysorbate 20 (Tween®20, Sigma-Aldrich, Germany) was previously dissolved in the aqueous phase to stabilize the oil droplets. Glycerol (VWR Chemicals, France) was used to modify the aqueous phase viscosity.

2.2 Open-cell foams characteristics

Three grades of Nickel-Chrome alloy open-cell solid foam blocks were purchased from RECEMAT (Netherlands), with the commercial references NC1723, NC2733 and NC4753, referred to in this study as BP (big pores), MP (medium pores) and SP (small pores) respectively (Table 1). The foam blocks were analysed thanks to X-ray microtomography (GE Phoenix v|tome|x s, RX tube of 160 kV with a focal point of up to 1 µm), with a spatial resolution of 6 µm. The tomographic data were processed with the iMorph software providing illustrative 3D images of the samples (a typical reconstruction is provided in Figure 1) and a precise and statistical description of the structures (Table 1), including the geometrical specific surface area (a_g), open porosity (φ), cell diameters ($d_{\mathrm{cell},1,2}$) and the window diameter (d_{win}). For the mean cell/pore diameter, two methods were used, giving different results (Table 1). The first one, $d_{\mathrm{cell},1}$, is based on the determination of a sphere having an equivalent volume as the cell. The second one, $d_{\mathrm{cell},2}$, is determined considering the maximum sphere included in the cell. Several cylinders of these foam blocks (with a diameter $d_{\mathrm{OCSF}} = 4.5$ mm, and a length $L = 25$ mm) were precisely cut using an electric arc discharge machining. These cylinders were then inserted in transparent flexible plastic tubes. Their diameter was calculated to ensure no bypass of the fluid near the wall region. Several cylinders could be inserted in series to study the effect of the mixing length.

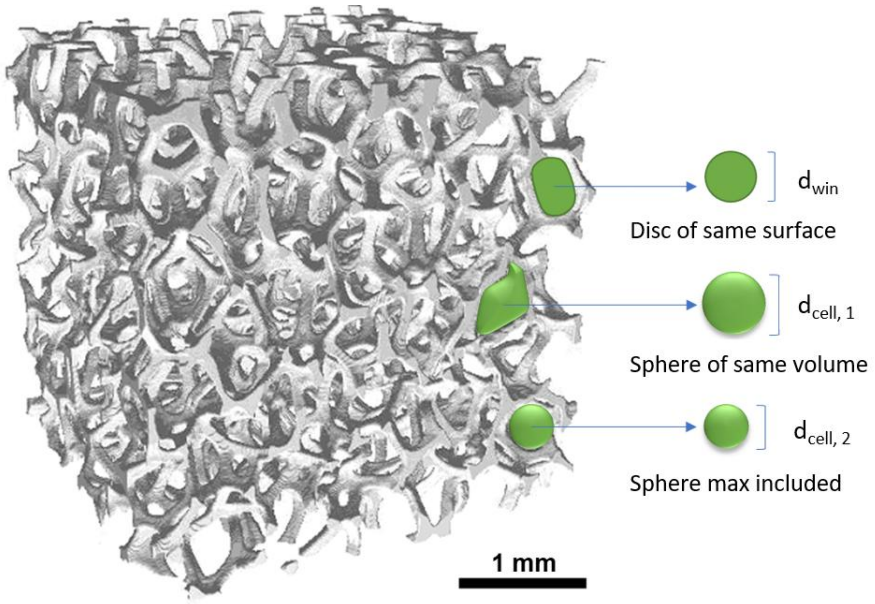

Figure 1: Typical tomography X reconstruction and visualization of the characteristic lengths.

Table 1: Geometrical features of the 3 NiCr foams determined with X-ray microtomography and image analysis. SMX+ properties were given by the supplier (Sulzer).

Property	**Comment**	**NC1723 (BP)**	**NC2733 (MP)**	**NC4753 (SP)**	**SMX+**
Pores per inch (PPI)	Supplier data	20	30	50	/
Specific surface area, a_g (m^2/m^3)	-	2 170±40	3 010±50	4 060±70	1527
Open porosity, φ (%)	-	91	90	88	75
Cell diameter, $d_{cell,1}$ (mm)	Equivalent sphere of the same volume	1.50±0.25	1.03±0.1	0.74±0.14	/
Cell diameter, $d_{cell,2}$ (mm)	The biggest sphere inscribed in the cell	1.16±0.28	0.79±0.12	0.60±0.12	/
Window diameter, d_{win} (mm)	Equivalent disc of the same surface	0.72±0.290	0.21±0.14	0.17±0.05	/
Hydraulic diameter, D_h (mm)	$D_h = \frac{4\varphi}{a_g}$	1.677±0.032	1.196±0.034	0.867±0.016	1.42

2.3 Emulsions preparation and characterization

The emulsification process is described in Figure 2. The OCSF cylinders previously cut were inserted into transparent plastic tubing of 5 mm internal diameter. The total length of the foam depends on the number of inserts which was varied during the study for the three different foams. For comparison purposes, SMX+ static mixers (from Sulzer) were also employed as

inserts. The properties of these classical mixers are given in Table 1 [29]. The Tween®20 surfactant was dissolved in the aqueous phase at a concentration of 5 g L^{-1}. This concentration, besides the high dilution conditions, is sufficient to ensure the stability of the oil droplets against coalescence [16,30]. The oil and the water solution were pumped separately using MCP-Z Ismatec gear pumps through the porous media in which droplet breakage occurs. A pressure gauge (Keller LEO1: 0–3 bar, ± 3 mbar, Germany) was installed upstream of the inserts for pressure drop measurement during emulsification. The oil phase fraction was kept constant at 1 wt %. Because of this low fraction, the oil phase was introduced parallel to the aqueous phase using a needle as depicted in Figure 2 to avoid the counter-pressure of the continuous phase to cause any oscillations in the oil phase flow rate. The prepared O/W emulsion taken downstream of the system was analysed using laser diffraction (Mastersizer 3000, Malvern Instruments, France) for DSD measurement after significant dilution in water. The interfacial tension was measured by a Drop Shape Analysis System DSA10 Mk2 (Krüss GmbH, Germany). All the experiments and the analysis were conducted at 20 °C.

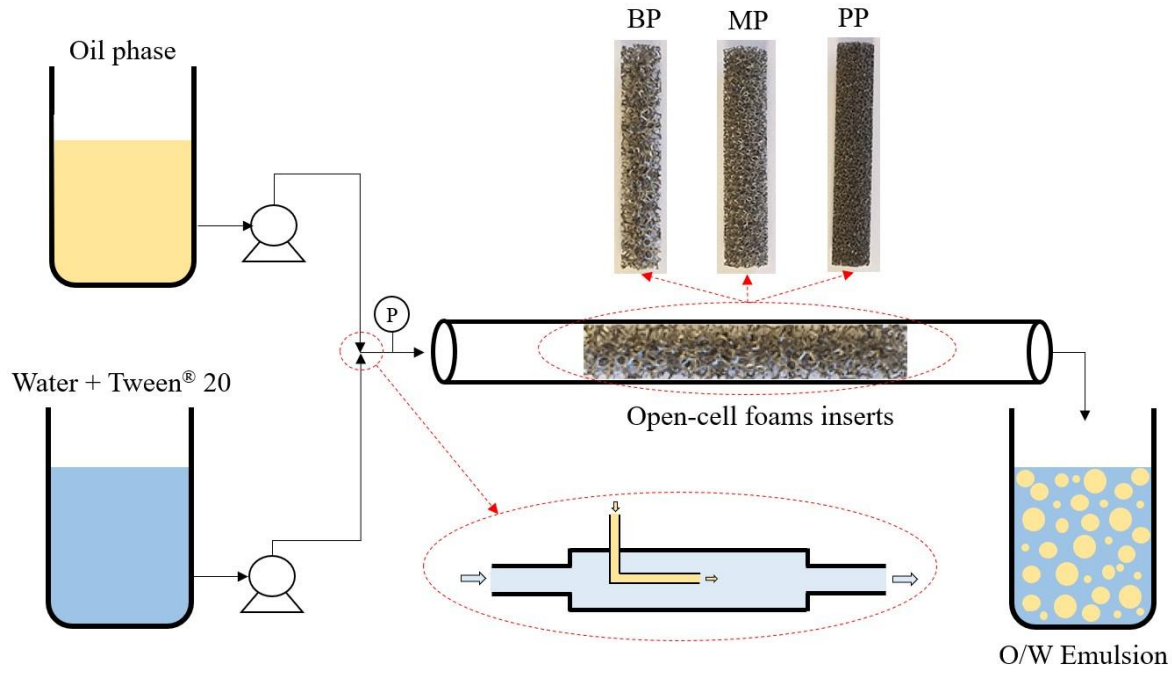

Figure 2: Schematic representation of the metallic open-cell foam-based emulsification system.

The investigated parameters were the length of the inserts which was varied from $L = 25$ mm to $L = 325$ mm, the viscosity of the dispersed phase (10, 50 and 350 mPa s), the viscosity of the continuous phase (1, 5 and 10 mPa s) and the superficial velocity from $u_s = 0$ to $u_s = 1.5$

m s^{-1}. These parameters were investigated for the three foam types. The characteristics of the continuous phase are given in Table 2.

Table 2: Characteristics of water-glycerol mixtures employed as continuous phase in the study.

Mixture N°	Viscosity, μ (mPa s)	density, ρ (kg m^{-3})	Glycerol content (g L^{-1})
1	1	998	0
2	5	1117	457
3	10	1150	578

The pressure drops induced by the different inserts were measured in a single-phase aqueous flow using the three water-glycerol mixtures (Table 2) at different superficial velocities. It is worth noting that, since the dispersed phase fraction is 1 wt % in the different emulsification tests, the contribution of the dispersed phase to pressure drop is negligible.

3 Theoretical background

3.1 Pressure drops prediction

Pressure drop measurements in each static mixer type are analysed using the Darcy-Forchheimer approach [31,32], well-known in the field of porous media. It is well suited for the fitting of pressure drop curves when viscous and inertia terms coexist (equation 1).

$$\frac{\Delta p}{L} = \frac{1}{k_1}\mu_c u_s + \frac{1}{k_2}\rho_c u_s^2 \quad (1)$$

where ΔP is the pressure drop, μ_c and ρ_c are the dynamic viscosity and the density of the continuous phase respectively, k_1 and k_2 are the permeability and the passability (or inertial permeability) of the porous media respectively.

In this equation, k_1 (m^2) and k_2 (m) are intrinsic parameters characteristic of the porous media. Their determination is carried out by a classic least squares regression of the experimental results. The highest are these coefficients, the lowest are the corresponding pressure drop terms. They allow a direct and easy comparison of different porous media. Knowing these two coefficients and the physical properties of the fluid flow allows to predict the pressure drop and the corresponding energy dissipation rate (see eq. 3 in the next section).

3.2 Mean droplet size prediction

Since decades, correlations have been developed to predict the mean droplet size in different emulsification processes [15,33]. Under turbulent conditions, these correlations are generally based on the Kolmogorov-Hinze theory of turbulence [34,35]. Assuming a homogeneous and isotropic turbulence flow field, the droplet breakage is due to the inertial and viscous stresses acting on the droplet surface at different length scales depending on the droplet size and the size of the smallest turbulent eddies given by the Kolmogorov length scale η defined as [36]:

$$\eta = \left(\frac{\nu^3}{\varepsilon_{\mathrm{m}}}\right)^{\frac{1}{4}} \tag{2}$$

where ν is the kinematic viscosity of the system and ε_{m} is the mean turbulent energy dissipation rate.

In the case of packed pipes, the mean energy dissipation rate is accessible through the pressure drop measurement as [14]:

$$\varepsilon_{\mathrm{m}} = \frac{\Delta P u_{\mathrm{i}}}{\rho_{\mathrm{c}} L} \tag{3}$$

where u_{i} is the interstitial velocity of the fluid, calculated as:

$$u_{\mathrm{i}} = \frac{u_{\mathrm{s}}}{\varphi} = \frac{4Q}{\pi D^2}\frac{1}{\varphi} \tag{4}$$

where Q is the volumetric fluid flow rate and D the internal empty tube diameter.

Following the Kolmogorov-Hinze theory, the maximum stable droplet diameter (d_{max}) is generally expressed in terms of nondimensional numbers in the form below [15]:

$$\frac{d_{\mathrm{max}}}{D_{\mathrm{h}}} = C_1 We_{\mathrm{h}}^{\alpha} Re_{\mathrm{h}}^{\beta} \tag{5}$$

where C_1, α and β are adjusted parameters, We_{h} and Re_{h} are the hydraulic Weber and Reynolds numbers respectively, given respectively by:

$$We_{\mathrm{h}} = \frac{\rho_{\mathrm{c}} u_{\mathrm{s}}^2 D_{\mathrm{h}}}{\varphi^2 \sigma} \tag{6}$$

and

$$Re_{\mathrm{h}} = \frac{\rho_{\mathrm{c}} u_{\mathrm{s}} D_{\mathrm{h}}}{\varphi \mu_{\mathrm{c}}} \tag{7}$$

where σ is the interfacial tension.

The maximum stable droplet size is proportional to the mean droplet diameter (d_{pq}) such as [37]:

$$d_{pq} = C_2 d_{\max} \tag{8}$$

The mean droplet size (d_{pq}) is defined as:

$$d_{pq} = \left(\frac{\sum_i N_i d_i^p}{\sum_i N_i d_i^q}\right)^{\frac{1}{p-q}} \tag{9}$$

where p and q are positive integers, N_i is the number of droplets in the class i and d_i is the representative diameter of the class i. Two main mean droplet sizes are generally employed, the Sauter mean diameter (d_{32}) and the volume-based mean diameter (d_{43}).

Middleman (1974), first proposed a correlation for turbulent droplet breakage in Kenics-type static mixers following the form of equation 5 as [38]:

$$\frac{d_{32}}{D_\mathrm{h}} = C_3 We^{-0.6} Re^{0.1} \tag{10}$$

Later, Chen and Libby (1978) considered the viscosity ratio between the two phases [39] and different authors followed the same approach [40–43]. Because of the high viscosity ratio in our case (between 10 and 350), this parameter is considered and following the Middleman's framework, the correlation in equation 10 is reformulated as:

$$\frac{d_{43}}{D_\mathrm{h}} = C_4 We^{\alpha} Re^{\beta} \left(\frac{\mu_\mathrm{d}}{\mu_\mathrm{c}}\right)^{\gamma} \tag{11}$$

It is worth noting that other parameters may be considered such as the density ratio between the phases and the dispersed phase fraction [44,45]. In our specific case, the density ratio between the silicone oils and the aqueous phase is close to unity and the dispersed phase fraction is very low (1 wt %). Therefore, these two parameters are neglected.

4 Results and discussion

4.1 Pressure drops

The experimental pressure drop profiles obtained for the different static mixers and the three viscosities are presented in Figure 3 as a function of the superficial velocity. First, the change in the slope of the different curves when increasing the velocity reveals the non-negligible role of the inertial term on pressure drop. Its importance seems to decrease when the viscosity increases from 1 to 10 mPa s, so more linear curves are obtained. The inflection shows the

passage from a laminar flow to a turbulent flow. In all cases, turbulent conditions are obtained after 0.5 m s^{-1} except for SP at high continuous phase viscosity ($\mu_c > 1$ mPa s). Logically, for a given fluid, the highest is the specific surface area of the OCSF mixer, the higher is the linear pressure drop. Finally, it is interesting to notice the relative position of the reference SMX+ mixer pressure drop curve in comparison to the 3 OCSF behaviours. The SMX+ has an intermediate behaviour between the two foams having the medium and small pores (MP and SP).

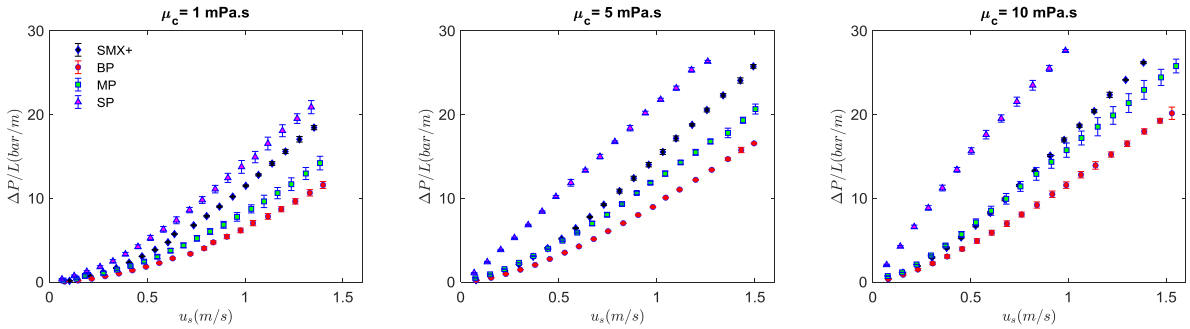

Figure 3: Experimental pressure drop within the open-cell foams (BP: big pores, MP: medium pores, SP: small pores) and SMX+ static mixers as a function of the fluid velocity at three different fluid viscosities.

Table 3 lists the regressed permeabilities and passabilities according to the Darcy-Forchheimer equation for the reference SMX+ and the three OCSF mixers (using eq. 1). All permeabilities and passabilities lie in the range of 10^{-8} m^2 and 10^{-3} m respectively, which are classical values for such foam media [46]. A focus on the 3 OCSF mixers indicates a logical gradual order of these two parameters according to the mean pore diameter or the geometrical specific surface area. Smaller permeability and passability are obtained with smaller pores. The permeability of SMX+ mixers is comparable to BP while its passability is comparable to SP.

Table 3: Permeabilities and passabilities of the different mixers in the Darcy-Forchheimer equation.

Static mixers	**Permeability k_1 (m^2)**	**Passability k_2 (m)**	**Mean relative error (-)**
SMX+	1.78×10^{-8}	1.03×10^{-3}	9 %
BP	2.07×10^{-8}	1.81×10^{-3}	7 %
MP	1.37×10^{-8}	1.53×10^{-3}	11 %
SP	0.49×10^{-8}	0.97×10^{-3}	14 %

Figure 4 presents a parity plot of the pressure drops regressed using the Darcy-Forchheimer equation with the experimental values. The points are close to the $y = x$ curve and are quasi always within the ±30 % window, which indicates a good ability to capture and predict the pressure drop by this approach. The mean relative errors of 7 % to 14 % between the calculated and experimental values for all the mixers (Table 3) confirm quantitatively this trend.

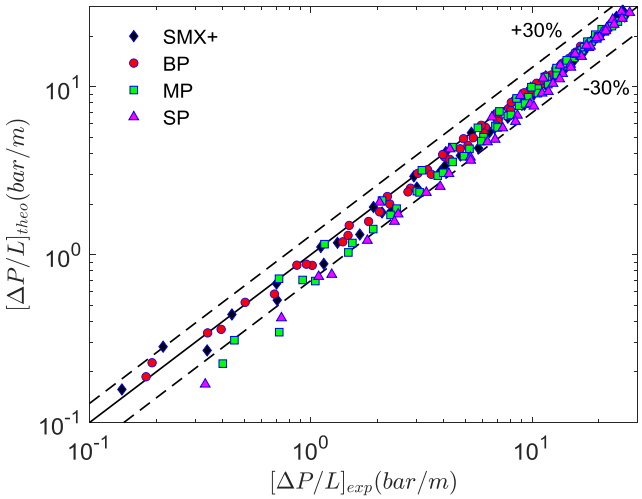

Figure 4: Parity plot of the pressure drops for the four mixers under different conditions.

4.2 Effect of the packing length on the emulsion quality

The effect of the foam inserts length (L) on the oil dispersion was investigated by varying it between 25 mm (1 insert) and 325 mm (13 inserts) for the three foams while keeping the same oil viscosity ($\mu_d = 10$ mPa s), continuous phase viscosity ($\mu_c = 1$ mPa s) and superficial velocity ($u_s = 0.6$ m s^{-1}). As shown in Figure 3, a turbulent flow regime was reached at $u_s > 0.5$ m s^{-1} (Figure 3). All the results reported in this study are exclusively related to turbulent emulsification. The results of the effect of L on the liquid-liquid dispersion are given in Figure 5.

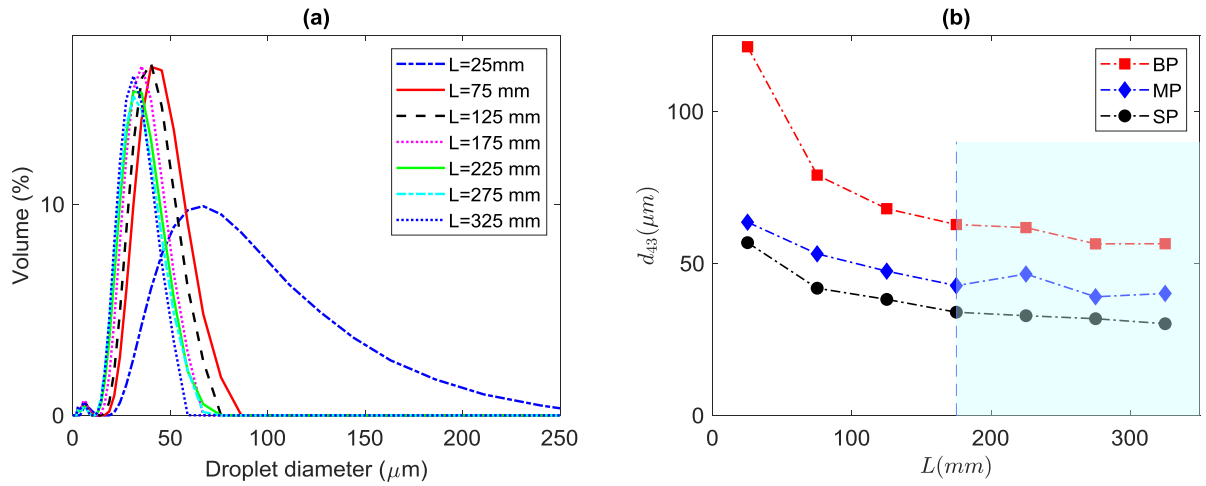

Figure 5: (a) Experimental DSD evolution with different total lengths of the foam inserts (L) in the case of SP foams; (b) Evolution of the experimental volume-based mean diameter d_{43} as a function of the OCSF length for the three different foams (with $\mu_d = 10$ mPa s, $\mu_c = 1$ mPa s, $u_s = 0.6$ m s^{-1}).

Figure 5-a shows the DSD evolution obtained with the SP foam at different packing lengths. At $L = 25$ mm, a broad DSD with a long tail is formed showing the beginning of the emulsification process. From $L = 25$ mm to $L = 75$ mm, the DSD shifts considerably toward smaller sizes and becomes narrower which demonstrates the high efficiency of these initial foam inserts (2nd and 3rd) to break down the oil droplets. From $L = 75$ mm to $L = 175$ mm, the DSD continues to shift toward smaller sizes but at a reduced rate while conserving the same shape. This trend was also observed with the other foams (MP and BP), where in all the cases with $L > 175$ mm, the DSD is almost constant showing that at this length, a stationary state is reached. In Figure 5-b, the d_{43} is reported for the three foams against the length of the foam inserts. A rapid decrease in the d_{43} is highlighted at $L \leq 75$ mm, a moderate decrease for $75 < L < 175$ mm and a stabilization for $L > 175$ mm. These results agree with those reported in the literature by Luo et al. (2017) [22].

Regarding the efficiency of the different foams, Figure 5-b shows also that under the same conditions, whatever the foam length, $d_{43}(\text{SP}) < d_{43}(\text{MP}) < d_{43}(\text{BP})$, which means that the SP foam is more efficient to break the oil droplets than MP and BP foams. This is due to the reduced size of the pores which induce more pressure drop and more energy dissipation. However, it is clear from Figure 5-b that the d_{43} results obtained with the MP foam are close to those obtained with the SP foam despite the difference in pressure drop induced by both foams. Figure 6 compares the DSDs from the different foams, at $L = 175$ mm where they reach equilibrium. The DSD of the emulsion prepared using the MP foam is close to the SP foam, and both foams generate a narrower distribution compared to the BP foam.

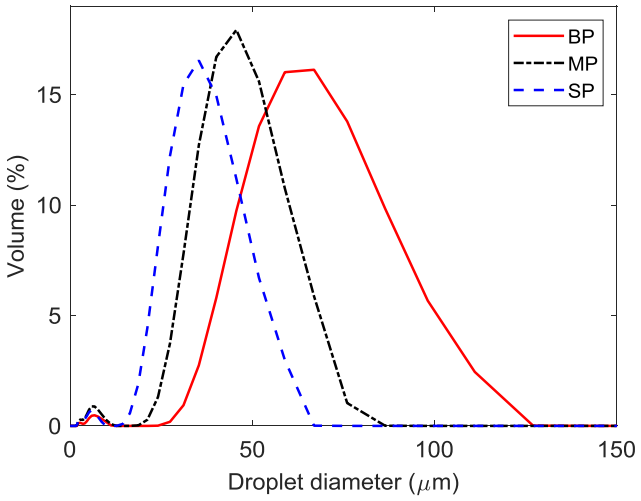

Figure 6: Comparison of the experimental DSDs obtained with the three foams using the same oil of $\mu_d = 10$ mPa.s, the same velocity of $u_s = 0.6$ m s^{-1} at $L = 175$ mm.

4.3 Effect of the viscosity of the dispersed phase

The effect of the dispersed phase viscosity on the quality of the emulsions prepared using the three OCSFs is investigated in this section. To do so, the superficial velocity was kept constant at $u_s = 0.6$ m s^{-1} while the total length of the foam inserts was varied. Three different oils were tested with a dynamic viscosity ranging from 10 to 350 mPa s. The results are shown in Figure 7.

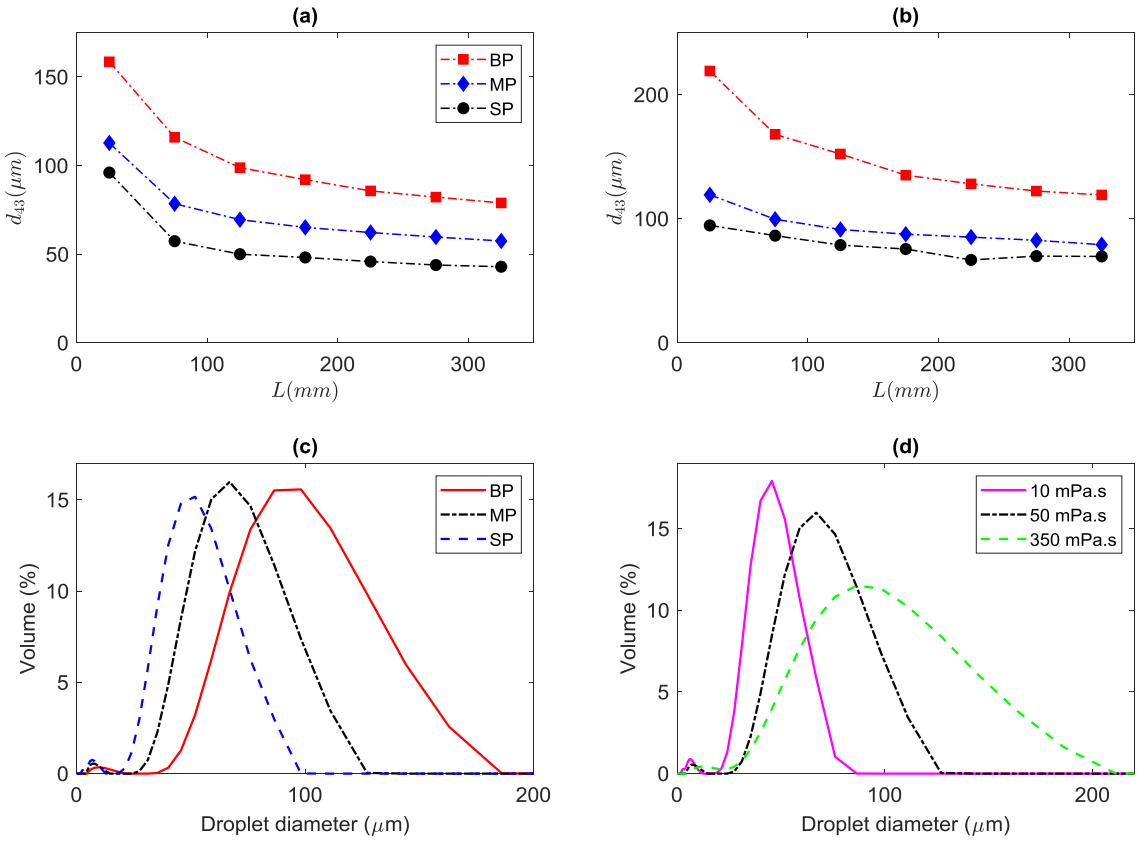

Figure 7: Evolution of the experimental d_{43} as a function of the length of the OCSF inserts for the three different foams using oils of $\mu_d = 50$ mPa.s (a) and $\mu_d = 350$ mPa.s (b); experimental DSDs obtained at $L = 175$ mm and $\mu_d = 50$ mPa.s with the three different foams (c); experimental DSDs obtained at $L = 175$ mm using the MP foam with different oil viscosities (d). The fluid velocity is $u_s = 0.6$ m s^{-1} for the different plots.

The same trend reported in Figure 5-b is shown in Figure 7-a and Figure 7-b for $\mu_d = 50$ mPa s and $\mu_d = 350$ mPa s respectively, where a rapid decrease of the d_{43} is observed after the first inserts followed by a quasi-stagnation at $L > 175$ mm. The results of MP and SP foams are very close while the BP foam is less efficient. A clear shift toward the high sizes is discernible as the viscosity of the dispersed phase increases. This is explained by the increased cohesion of the droplets against the deforming and disrupting eddies. It is worth noting that the surface forces are equivalent in the different cases ($\sigma \approx 8.5$ mN m^{-1}) since all the experiments were prepared using the same surfactant and at the same concentration, and the pressure drop is not impacted by the dispersed phase viscosity since its fraction is very low (1 wt %).

Figure 7-c compares the experimental DSDs obtained with the three foams at $L = 175$ mm and $\mu_d = 50$ mPa s. The SP foam is very efficient and allows to prepare an emulsion with

$d_{43} = 48$ µm followed by the MP foam with $d_{43} = 65$ µm and finally the BP foam with $d_{43} = 92$ µm. Figure 7-d shows the DSD results of the MP foam for the three different oils with a packing length of 175 mm. As the oil viscosity increases, the DSD becomes broader and shifts toward the high sizes for the same reasons explained earlier.

4.4 Effect of the fluid flow rate

The effect of the flow rate of the continuous phase is investigated by carrying out the emulsification experiments at different superficial velocities ranging from $u_s = 0.6$ m s^{-1} to $u_s = 1.2$ m s^{-1}. Within this range, turbulent emulsification is achieved. The results are given in Figure 8.

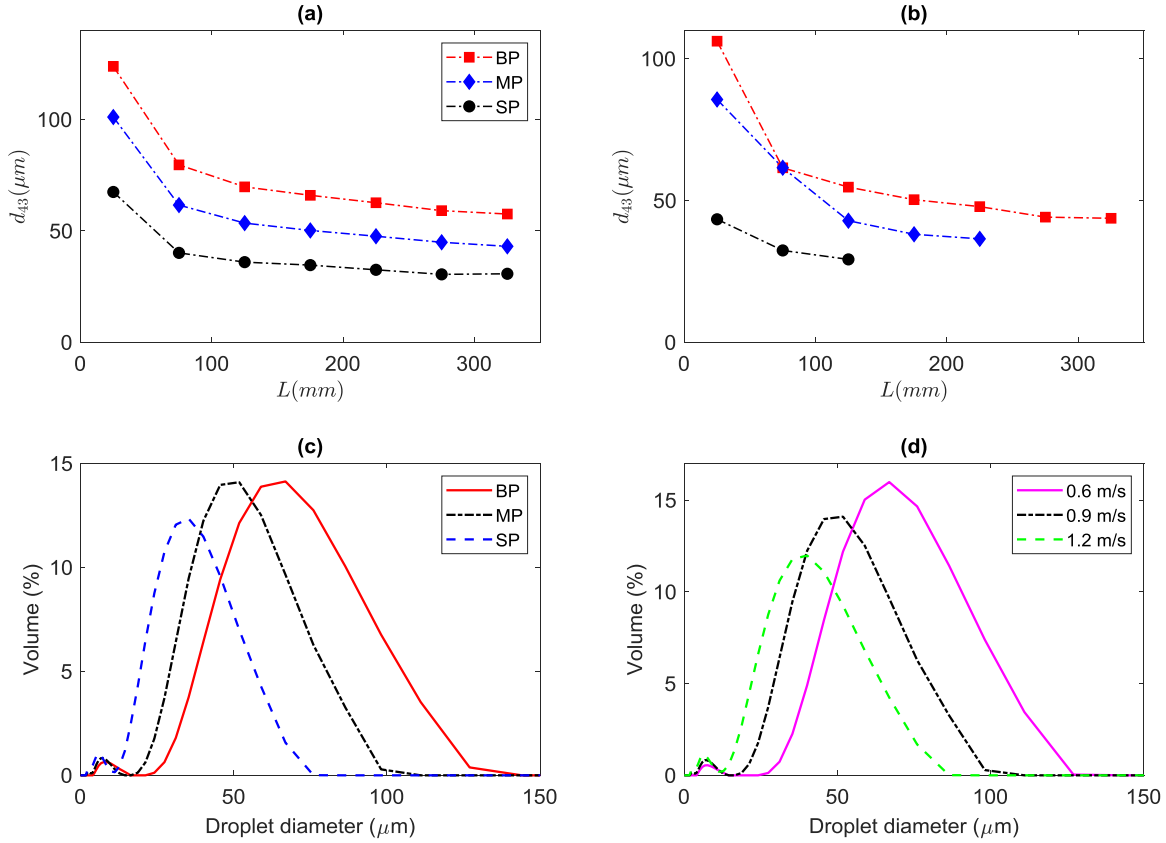

Figure 8: Evolution of the experimental d_{43} as a function of OCSFs length for the three different foams at $u_s = 0.9$ m s^{-1} (a) and $u_s = 1.2$ m s^{-1} (b); experimental DSDs obtained with L=175 mm for the three different foams at $u_s = 0.9$ m s^{-1} (c); experimental DSDs obtained with L=175 mm using the MP foam at different fluid velocity. The fluid viscosity is $\mu_d = 50$ mPa s for the different plots.

The evolution of the d_{43} as a function of the foam length at superficial velocities of $u_s = 0.9$ m s^{-1} and $u_s = 1.2$ m s^{-1} is reported in Figure 8-a and Figure 8-b respectively. For the MP and SP foams at $u_s = 1.2$ m s^{-1}, the data at high L is missing because the pressure drop exceeded

3 bars which is the maximum of the pressure gauge used in this study. Increasing the superficial velocity increases the pressure drop and the energy dissipation rate leading to more droplet breakage intensity. It is clear that the emulsions stabilize at smaller sizes than previously observed at a lower velocity. The DSDs become narrower and are shifted toward smaller sizes, as reported in Figure 8-c comparing the foams at $u_s = 0.9$ m s^{-1} and $L = 175$ mm, and Figure 8-d comparing the three velocities for the MP foam at $L = 175$ mm.

4.5 Emulsification at the same mean energy dissipation rate

As introduced in the theoretical background section, one crucial parameter in mixing processes is the energy dissipation rate (ε). As in the classical static mixers, due to the spatial confinement of the system and the random cris-cross fluid flows within the OCSFs, the energy dissipation rate is more homogeneous than in stirred tanks for instance and the mean energy dissipation rate (ε_m) estimated from the pressure drop may be used as a good approximation of the local energy dissipation rate [30].

To maintain the same mean energy dissipation rate around $\varepsilon_m = 500$ m^2 s^{-3} when using the different foams, the flow rate is adjusted leading to a superficial velocity of $u_s = 0.89$ m s^{-1} for the BP foam, $u_s = 0.79$ m s^{-1} for the MP foam and $u_s = 0.67$ m s^{-1} for the SP foam. The results at steady-state (for $L = 175$ mm) are given in Figure 9.

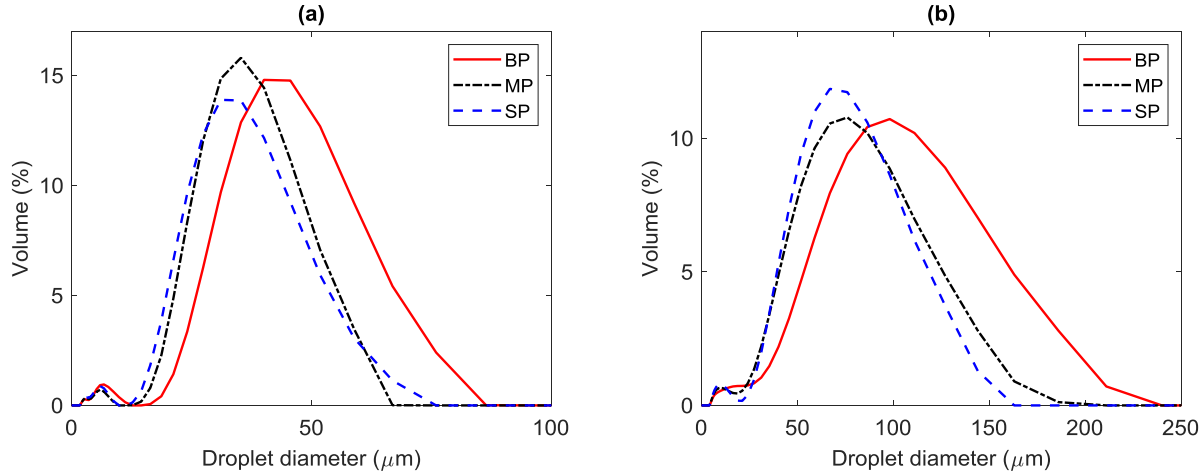

Figure 9: Comparison between the experimental DSDs obtained using the three foams at $L = 175$ mm and $\varepsilon_m = 500$ m^2 s^{-3} for the oils of $\mu_d = 10$ mPa s (a) and $\mu_d = 350$ mPa s (b).

It was expected that the foams would have the same breakage efficiency when the same amount of energy is dissipated in the system. Indeed, most kernels of droplet breakage in the turbulent regime are based on the energy dissipation rate, even though other semi-empirical kernels use the Reynolds number. However, it can be seen in Figure 9 that only the SP and

MP foams lead to almost the same DSD at the same energy dissipation rate, whatever the dispersed phase viscosity, while the BP foam is clearly less efficient. This distinction may be related to the high difference between the BP foam on one side and the other foams in terms of pore size (Table 1). Even if the global porosity is very close for the three foams, the mean size of the pores decreases from $d_{\mathrm{cell},1} = 1.50$ mm for the BP foam to 1.03 mm for the MP, and 0.74 mm for the SP foam. This impacts the local fluid mixing quality and the hypothesis of homogeneity of the energy dissipation rate which is directly related to the emulsification efficiency. It is worth noting that under these conditions ($u_s = 0.79$ m s^{-1} for MP and $u_s = 0.67$ m s^{-1} for SP), the pressure drop induced by the SP foam ($\Delta P = 1.13$ bar) was still higher than that of the MP foam ($\Delta P = 1.00$ bar) but both systems lead to the same DSD.

Luo et al. (2017) correlated the Sauter mean diameter directly to the mean energy dissipation rate in the case of a helical tube reactor with a premixing tube filled with solid foams [22]. Following the same procedure, Figure 10 shows the evolution of the d_{43} as a function of the mean energy dissipation rate (ε_{m}) at steady state ($L = 175$ mm) including the results of the three foams. It is clear from Figure 10 that in our case, focusing only on the mean energy dissipation rate (ε_{m}) cannot explain the experimental trend of the mean droplet size, as different diameters where observed at the same ε_{m} in the big pores compared to the other pores for instance.

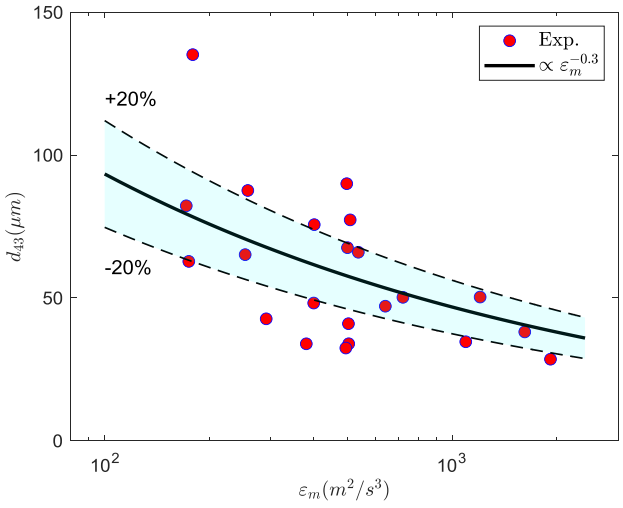

Figure 10: Mean droplet size (d_{43}) as a function of the mean energy dissipation rate (ε_{m}).

4.6 OCSFs *versus* SMX+ static mixers

To assess the emulsification performances of the different OCSFs employed in this study, the results are compared to those obtained using SMX+ static mixers in the same conditions of

superficial velocity ($u_s = 0.6$ m s^{-1}) and total length of the inserts ($L = 75$ mm). The comparison is given in Figure 11 in terms of DSD for the three different oils.

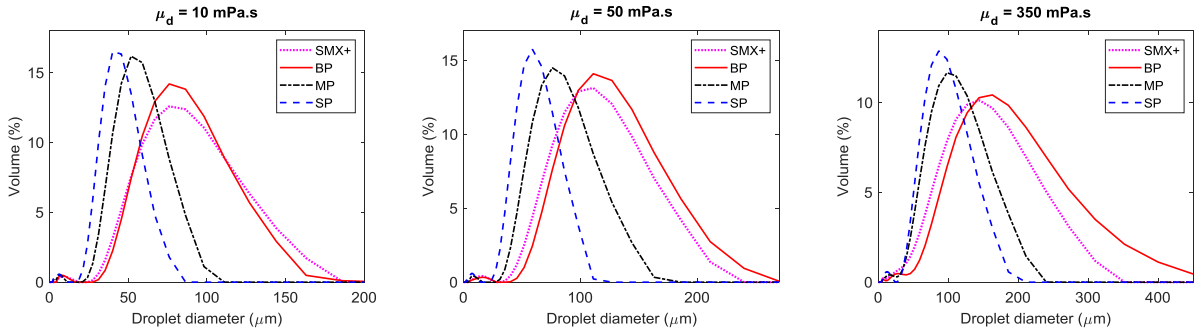

Figure 11: Comparison of the DSDs obtained with the different foams with the SMX+ static mixers, using three different oil viscosities. The total length of the inserts is $L = 75$ mm and the fluid velocity $u_s = 0.6$ m s^{-1}.

As reported in Figure 3, at the fluid velocity of $u_s = 0.6$ m s^{-1}, only the pressure drop of the SP foam is higher than that of the SMX+ static mixers. If we assume that, for a specific velocity, the pressure drop will determine the droplet breakage rate, then it is expected that only the SP foam will be more performant than SMX+ mixers. However, as shown in Figure 11, the BP foam and the SMX+ mixers have almost the same performance, for the three different oils. It is important to remember that $\Delta P = 0.20$ bar for BP and $\Delta P = 0.24$ bar for SMX+ at this velocity. More interestingly, the MP foam leads to a considerable shift of the DSD toward the small sizes. For highly viscous oils, the MP foam shows a very good emulsification performance, almost comparable to the SP foam.

The superior emulsification performances of the OCSFs compared to SMX+ static mixers are explained by the geometrical properties of these solid foams which offer more porosity with smaller pores and the spatial random connexions of the pores unlike in SMX+ static mixers in which the crossed bars divide and recombine the fluid flow consistently in the same way.

4.7 Prediction of the mean droplet size at equilibrium

As introduced earlier, many correlations exist in the literature regarding the prediction of the mean droplet size at equilibrium in continuous emulsification systems. Hereafter, the original correlation proposed by Middleman is tested. It relies only on one parameter (C_3 of equation 10) that is identified using a global optimization procedure (least square minimization) over the different experiments at equilibrium including the three foams without distinction. The results are given in Figure 12-a and in Table 4.

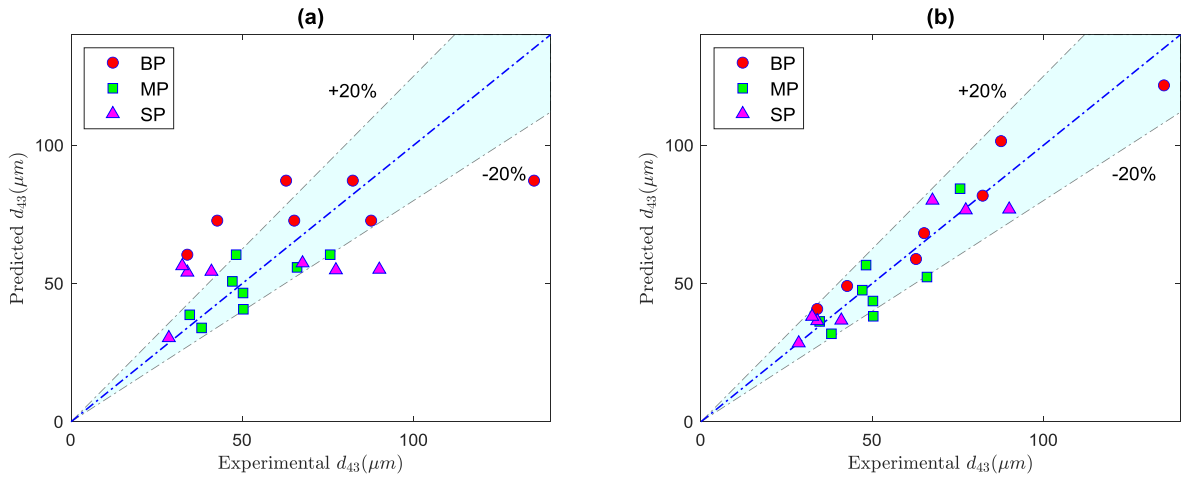

Figure 12: Comparison between the predicted and the experimental d_{43}: (a) using the Middleman correlation (equation 10, with C_3 being identified), (b) using the Middleman correlation with viscosity ratio correction (equation 11, with C_3 and γ being identified).

As shown in Figure 12-a, the predictions of the Middleman's correlation in our case are not accurate since different experimental results are over/under-predicted out of the interval of confidence of ±20 % except for the MP foam.

To enhance the predictability of the previous correlation, the viscosity correction is introduced (see equation 11) without changing the power coefficients of the Middleman's correlation ($\alpha = -0.6$ and $\beta = 0.1$). Two parameters are identified in this case (C_3 and γ given in Table 4). The results are given in Figure 12-b. Introducing the viscosity correction improves considerably the predictability of the correlation. All the experimental d_{43} are predicted within the interval of ±20 %. This is explained by the wide range of variations of the dispersed phase viscosity. The optimized power coefficient is $\gamma = 0.2$, which is consistent with that obtained by Chen and Libby (1978) in the case of emulsification using Kenics-type static mixers ($\gamma = 0.18$) [39].

For further improvement of the correlation, its four parameters are now optimized (equation 11). The results in terms of mean size predictability are given in Figure 13 and the numerical values of the fitted parameters are reported in Table 4.

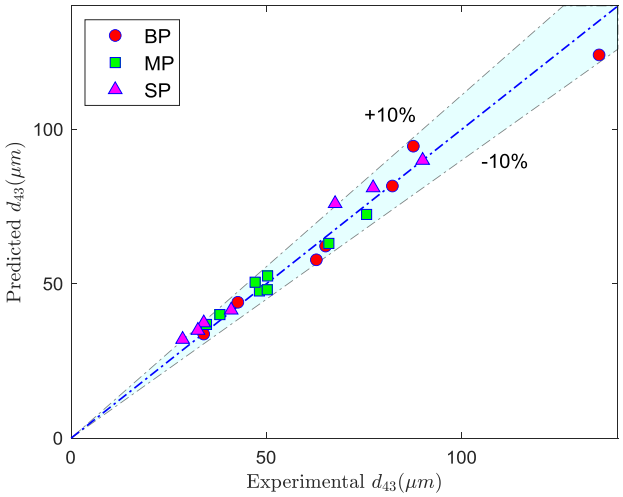

Figure 13: Comparison between the predicted and the experimental d_{43} using the Middleman correlation with viscosity correction and parameters optimization (equation 11, with 4 parameters being identified).

The optimization of the different parameters of the correlation in equation 11 further refines the predictions as shown in Figure 13. The predictions in this case are excellent with an error in the range of only ±10 % for all the experiments. The obtained power coefficients in this case are close to those obtained by Streiff (1977) in the case of emulsification using SMV static mixers ($\alpha = -0.5$ and $\beta = 0.15$) without viscosity correction [47].

Table 4: Summary of the different used correlations with the fitted parameters.

Correlation	**Identified parameters**
$\frac{d_{43}}{D_{\mathrm{h}}} = C_3 We^{-0.6} Re^{0.1}$	C_3 =0.37
$\frac{d_{43}}{D_{\mathrm{h}}} = C_3 We^{-0.6} Re^{0.1} \left(\frac{\mu_{\mathrm{d}}}{\mu_{\mathrm{c}}}\right)^{\gamma}$	$C_3 = 0.16$, $\gamma = 0.2$
$\frac{d_{43}}{D_{\mathrm{h}}} = C_4 We^{\alpha} Re^{\beta} \left(\frac{\mu_{\mathrm{d}}}{\mu_{\mathrm{c}}}\right)^{\gamma}$	$C_4 = 0.03$, $\alpha = 0.42$, $\beta = 0.20$, $\gamma = 0.22$

5 Conclusions

This study reported the liquid-liquid emulsification capability of three open-cell solid foams. These metal foams have almost the same global porosity but distinct geometrical properties.

First, the pressure drop induced by the different porous media is measured experimentally showing a non-negligible role of the inertial term. The effect of the inertial term decreases as the viscosity of the continuous phase increases. The pressure drop increases for increasing the specific surface area of the OCSF. The SMX+ mixers showed a pressure drop between the MP and the SP foams. The classical Darcy-Forchheimer equation allowed to capture and predict the pressure drop profiles with a mean relative error of 14 % at most.

O/W emulsions were then prepared under different conditions, by parallel pumping of the two phases through a packed pipe with different packing lengths, superficial velocities and viscosities of the continuous/dispersed phases. In all the cases, the DSD is shown to undergo a strong evolution (narrowing and shifting toward small sizes) within the first inserts before stabilizing at $L \geq 175$ mm. Monomodal DSDs are obtained with the smallest mean diameter for the SP foam followed by the MP foam and the BP foam respectively at constant superficial velocity. This is explained by the higher pressure drop induced by the SP foam which means that more energy is dissipated in the system. However, when working at the same mean energy dissipation rate, the performances of the SP and MP foams are equivalent and higher than those of the BP foam. The MP foam is so considered to be the most performant since it leads to the same DSD as the SP foam with less pressure drop.

The OCSF emulsification capabilities are compared to those obtained using classical structured static mixers (SMX+) at the same length and superficial velocity. The SMX+ mixers exhibit the same breakage performance as the BP foam for the different oils while the MP and SP foams are more efficient and lead to smaller droplets. One should recall that under these conditions, only the SP foam induces a pressure drop higher than that of the SMX+ mixers.

Last, the Middleman's correlation for the mean droplet size prediction at equilibrium is tested showing that, because of the high difference between the oils in terms of viscosity, the viscosity ratio between the dispersed and the continuous phases should be considered for more accurate predictions. Moreover, the re-estimation of the Middleman's correlation parameters with viscosity correction leads to excellent predictions for the three foams under the different conditions with errors less than 10 % in all the cases.

Nomenclature

a_{g}	Specific surface area	$m^2 m^{-3}$
C_i	Constants	-
D	Internal diameter of the pipe	mm
$d_{\mathrm{cell},1}$	Cell diameter calculated as the diameter of the equivalent sphere of the same volume	μm
$d_{\mathrm{cell},2}$	Cell diameter calculated as the diameter of the biggest sphere inscribed in the cell	μm
D_{h}	Hydraulic diameter of the packed pipe	mm
d_i	Representative diameter of the class *i*	μm
$d_{\max}$	Maximum stable droplet diameter	μm
d_p	The mean pore diameter of the foams	μm
d_{OCSF}	Diameter of the open-cell solid foam inserts	mm
d_{pq}	Droplet mean diameter	μm
d_{win}	Window diameter calculated as the diameter of the equivalent disc of the same surface as that of the pores	μm
d_{32}	Sauter mean diameter	μm
d_{43}	Volume-based mean diameter	μm
k_1	Permeability of the porous media	m^2
k_2	Passability of the porous media	m
L	Length of the open-cell metal foam inserts	mm
N_{i}	Number of droplets in the class *i*	m^{-3}
u_{i}	Interstitial velocity of the fluid	$m\ s^{-1}$

u_s	Superficial velocity of the fluid	m s^{-1}
p, q	Positive integers	-
ΔP	Pressure drop	Pa
Q	Volume flow rate of the fluid	m^3 s^{-1}
Re_h	Hydraulic Reynolds number	-
We_h	Hydraulic Weber number	-

α, β, γ	Parameters of the correlations	-
ε	Turbulent energy dissipation rate	m^2 s^{-3}
ε_m	Mean turbulent energy dissipation rate	m^2 s^{-3}
η	Kolmogorov length scale	m
μ_c	Dynamic viscosity of the continuous aqueous phase	mPa s
μ_d	Dynamic viscosity of the dispersed oil phase	mPa s
ν	Kinematic viscosity of the system	m^2 s^{-1}
ρ_c	Continuous phase density	kg m^{-3}
σ	Interfacial tension of the system	N m^{-1}
φ	Global porosity of the foam	-

Acknowledgement

This work was partially funded by Agence Nationale de la Recherche under the grant agreement ANR-22-CE51-0006-01 (DEPMod Project).

References

[1] M. Ambrosetti, M. Bracconi, M. Maestri, G. Groppi, E. Tronconi, Packed foams for the intensification of catalytic processes: assessment of packing efficiency and pressure drop using a combined experimental and numerical approach, Chemical Engineering Journal 382 (2020) 122801. https://doi.org/10.1016/j.cej.2019.122801.

[2] K. Pangarkar, T.J. Schildhauer, J.R. van Ommen, J. Nijenhuis, F. Kapteijn, J.A. Moulijn, Structured Packings for Multiphase Catalytic Reactors, Ind. Eng. Chem. Res. 47 (2008) 3720–3751. https://doi.org/10.1021/ie800067r.
[3] J. Lévêque, D. Rouzineau, M. Prévost, M. Meyer, Hydrodynamic and mass transfer efficiency of ceramic foam packing applied to distillation, Chemical Engineering Science 64 (2009) 2607–2616. https://doi.org/10.1016/j.ces.2009.02.010.
[4] J. Shi, G. Zheng, Z. Chen, C. Dang, Experimental study of flow condensation heat transfer in tubes partially filled with hydrophobic annular metal foam, International Journal of Heat and Mass Transfer 136 (2019) 1265–1272. https://doi.org/10.1016/j.ijheatmasstransfer.2019.03.039.
[5] J. Qu, Q. Sun, H. Wang, D. Zhang, J. Yuan, Performance characteristics of flat-plate oscillating heat pipe with porous metal-foam wicks, International Journal of Heat and Mass Transfer 137 (2019) 20–30. https://doi.org/10.1016/j.ijheatmasstransfer.2019.03.107.
[6] J.-N. Tourvieille, R. Philippe, C. de Bellefon, Milli-channel with metal foams under an applied gas–liquid periodic flow: External mass transfer performance and pressure drop, Chemical Engineering Journal 267 (2015) 332–346. https://doi.org/10.1016/j.cej.2014.11.084.
[7] J. Lévêque, R. Philippe, M.-L. Zanota, V. Meille, F. Sarrazin, L. Baussaron, C. de Bellefon, Hydrodynamics and mass transfer in a tubular reactor containing foam packings for intensification of G-L-S catalytic reactions in co-current up-flow configuration, Chemical Engineering Research and Design 109 (2016) 686–697. https://doi.org/10.1016/j.cherd.2016.03.017.
[8] C.P. Stemmet, J. Van Der Schaaf, B.F.M. Kuster, J.C. Schouten, Solid Foam Packings for Multiphase Reactors: Modelling of Liquid Holdup and Mass Transfer, Chemical Engineering Research and Design 84 (2006) 1134–1141. https://doi.org/10.1205/cherd05034.
[9] M. Bracconi, M. Ambrosetti, O. Okafor, V. Sans, X. Zhang, X. Ou, C.P. Da Fonte, X. Fan, M. Maestri, G. Groppi, E. Tronconi, Investigation of pressure drop in 3D replicated open-cell foams: Coupling CFD with experimental data on additively manufactured foams, Chemical Engineering Journal 377 (2019) 120123. https://doi.org/10.1016/j.cej.2018.10.060.
[10] A. Della Torre, G. Montenegro, G.R. Tabor, M.L. Wears, CFD characterization of flow regimes inside open cell foam substrates, International Journal of Heat and Fluid Flow 50 (2014) 72–82. https://doi.org/10.1016/j.ijheatfluidflow.2014.05.005.
[11] H. Yang, Y. Li, B. Ma, Y. Zhu, Review and a Theoretical Approach on Pressure Drop Correlations of Flow through Open-Cell Metal Foam, Materials 14 (2021) 3153. https://doi.org/10.3390/ma14123153.
[12] D.J. McClements, Food emulsions: principles, practices, and techniques, CRC press, 2015.
[13] M. Kaci, E. Arab-Tehrany, I. Desjardins, S. Banon-Desobry, S. Desobry, Emulsifier free emulsion: Comparative study between a new high frequency ultrasound process and standard emulsification processes, Journal of Food Engineering 194 (2017) 109–118. https://doi.org/10.1016/j.jfoodeng.2016.09.006.
[14] A. Ghanem, T. Lemenand, D. Della Valle, H. Peerhossaini, Static mixers: Mechanisms, applications, and characterization methods–A review, Chemical Engineering Research and Design 92 (2014) 205–228. https://doi.org/10.1016/j.cherd.2013.07.013.

[15] J.P. Valdés, L. Kahouadji, O.K. Matar, Current advances in liquid–liquid mixing in static mixers: A review, Chemical Engineering Research and Design 177 (2022) 694–731. https://doi.org/10.1016/j.cherd.2021.11.016.
[16] N. Lebaz, N. Sheibat-Othman, Population balance modelling of a continuous static mixer-based emulsification process, Chemical Engineering Research and Design 188 (2022) 645–654. https://doi.org/10.1016/j.cherd.2022.10.022.
[17] N. Lebaz, K. Touma, N. Sheibat-Othman, An original continuous process for double emulsions preparation using static mixers: Focus on the viscosity, Colloids and Surfaces A: Physicochemical and Engineering Aspects 674 (2023) 131984. https://doi.org/10.1016/j.colsurfa.2023.131984.
[18] R.K. Thakur, Ch. Vial, K.D.P. Nigam, E.B. Nauman, G. Djelveh, Static Mixers in the Process Industries—A Review, Chemical Engineering Research and Design 81 (2003) 787–826. https://doi.org/10.1205/026387603322302968.
[19] H.E.H. Meijer, M.K. Singh, P.D. Anderson, On the performance of static mixers: A quantitative comparison, Progress in Polymer Science 37 (2012) 1333–1349. https://doi.org/10.1016/j.progpolymsci.2011.12.004.
[20] R. Chakleh, F. Azizi, Performance comparison between novel and commercial static mixers under turbulent conditions, Chemical Engineering and Processing - Process Intensification 193 (2023) 109559. https://doi.org/10.1016/j.cep.2023.109559.
[21] I. Mohammed, T. Bauer, M. Schubert, R. Lange, Hydrodynamic multiplicity in a tubular reactor with solid foam packings, Chemical Engineering Journal 231 (2013) 334–344. https://doi.org/10.1016/j.cej.2013.07.024.
[22] J.-Z. Luo, G.-W. Chu, Y. Luo, H.-K. Zou, G.-J. Li, J.-F. Chen, Experimental investigations of liquid-liquid dispersion in a novel helical tube reactor, Chemical Engineering and Processing: Process Intensification 117 (2017) 162–170. https://doi.org/10.1016/j.cep.2017.04.002.
[23] L. Vanoye, B. Guicheret, C. Rivera-Cárcamo, R. Castro Contreras, C. de Bellefon, V. Meille, P. Serp, R. Philippe, A. Favre-Réguillon, Process intensification of the catalytic hydrogenation of squalene using a Pd/CNT catalyst combining nanoparticles and single atoms in a continuous flow reactor, Chemical Engineering Journal 441 (2022) 135951. https://doi.org/10.1016/j.cej.2022.135951.
[24] Z.-T. Wang, S.-X. Chen, Y. Ouyang, X.-Q. Zhang, B.-D. Zheng, N. Zhang, J. Ye, M.-T. Xiao, Y.-C. Yang, Intensification of Liquid–Liquid Emulsification Process in a Rotating Solid Foam Stirrer Tank: Experiments and Modeling, Ind. Eng. Chem. Res. 61 (2022) 14971–14982. https://doi.org/10.1021/acs.iecr.2c01951.
[25] Y.-C. Yang, S.-S. Zeng, Y. Ouyang, L. Sang, S.-Y. Yang, X.-Q. Zhang, Y.-Y. Huang, J. Ye, M.-T. Xiao, N. Zhang, An intensified ozonation system in a tank reactor with foam block stirrer: Synthetic textile wastewater treatment and mass transfer modeling, Separation and Purification Technology 257 (2021) 117909. https://doi.org/10.1016/j.seppur.2020.117909.
[26] R. Tschentscher, T.A. Nijhuis, J. van der Schaaf, J.C. Schouten, Glucose Oxidation in Slurry Reactors and Rotating Foam Reactors, Ind. Eng. Chem. Res. 51 (2012) 1620–1634. https://doi.org/10.1021/ie200694z.
[27] N. Lebaz, N. Sheibat-Othman, Population balance modelling of a continuous static mixer-based emulsification process, Chemical Engineering Research and Design 188 (2022) 645–654. https://doi.org/10.1016/j.cherd.2022.10.022.
[28] J. Hapanowicz, A. Szydłowska, K. Żak, Influence of the Presence of Metal Foam in a Horizontal Pipe on the Two-Phase Liquid-Liquid Mixture Flow Resistance, (2023). https://doi.org/10.2139/ssrn.4493767.

[29] N. Lebaz, N. Sheibat-Othman, Modeling Emulsification in Static Mixers: Equilibrium Correlations versus Population Balance Equations, Chemical Engineering & Technology 42 (2019) 1691–1701. https://doi.org/10.1002/ceat.201900109.
[30] N. Lebaz, F. Azizi, N. Sheibat-Othman, Modeling Droplet Breakage in Continuous Emulsification Using Static Mixers in the Framework of the Entire Spectrum of Turbulent Energy, Ind. Eng. Chem. Res. 61 (2022) 541–553. https://doi.org/10.1021/acs.iecr.1c03529.
[31] H. Darcy, Les fontaines publiques de la ville de Dijon exposition et application ... par Henry Darcy, Victor Dalmont, 1856.
[32] P. Forchheimer, Wasserbewegung durch boden., Zeitschrift Des Vereines Deutscher Ingenieure 45 (1901) 1781–1788.
[33] F. Theron, N. Le Sauze, Comparison between three static mixers for emulsification in turbulent flow, International Journal of Multiphase Flow 37 (2011) 488–500.
[34] A.N. Kolmogorov, Dissipation of energy in locally isotropic turbulence, in: Dokl. Akad. Nauk SSSR, 1941: pp. 16–18.
[35] J.O. Hinze, Fundamentals of the hydrodynamic mechanism of splitting in dispersion processes, AIChE Journal 1 (1955) 289–295. https://doi.org/10.1002/aic.690010303.
[36] N. Vankova, S. Tcholakova, N.D. Denkov, I.B. Ivanov, V.D. Vulchev, T. Danner, Emulsification in turbulent flow: 1. Mean and maximum drop diameters in inertial and viscous regimes, Journal of Colloid and Interface Science 312 (2007) 363–380. https://doi.org/10.1016/j.jcis.2007.03.059.
[37] F.B. Sprow, Distribution of drop sizes produced in turbulent liquid—liquid dispersion, Chemical Engineering Science 22 (1967) 435–442. https://doi.org/10.1016/0009-2509(67)80130-1.
[38] S. Middleman, Drop Size Distributions Produced by Turbulent Pipe Flow of Immiscible Fluids through a Static Mixer, Ind. Eng. Chem. Proc. Des. Dev. 13 (1974) 78–83. https://doi.org/10.1021/i260049a015.
[39] S. Chen, D. Libby, Gas-liquid and liquid-liquid dispersions in a Kenics mixer, Proceedings of the 71st Annual AIChE Meeting (1978).
[40] J.T. Davies, Drop sizes of emulsions related to turbulent energy dissipation rates, Chemical Engineering Science 40 (1985) 839–842. https://doi.org/10.1016/0009-2509(85)85036-3.
[41] R.V. Calabrese, T.P.K. Chang, P.T. Dang, Drop breakup in turbulent stirred-tank contactors. Part I: Effect of dispersed-phase viscosity, AIChE Journal 32 (1986) 657–666.
[42] E.W. Barega, E. Zondervan, A.B. de Haan, Influence of Physical Properties and Process Conditions on Entrainment Behavior in a Static-Mixer Settler Setup, Ind. Eng. Chem. Res. 52 (2013) 2958–2968. https://doi.org/10.1021/ie301580m.
[43] E. Chabanon, N. Sheibat-Othman, O. Mdere, J.P. Valour, S. Urbaniak, F. Puel, Drop size distribution monitoring of oil-in-water emulsions in SMX+ static mixers: Effect of operating and geometrical conditions, International Journal of Multiphase Flow 92 (2017) 61–69. https://doi.org/10.1016/j.ijmultiphaseflow.2017.03.001.
[44] S. Hirschberg, R. Koubek, F.Moser, J. Schöck, An improvement of the Sulzer SMX^{TM} static mixer significantly reducing the pressure drop, Chemical Engineering Research and Design 87 (2009) 524–532. https://doi.org/10.1016/j.cherd.2008.12.021.
[45] N.V. Rama Rao, M.H.I. Baird, A.N. Hrymak, P.E. Wood, Dispersion of high-viscosity liquid–liquid systems by flow through SMX static mixer elements, Chemical Engineering Science 62 (2007) 6885–6896. https://doi.org/10.1016/j.ces.2007.08.070.
[46] P. Khayargoli, V. Loya, L.-P. Lefebvre, M. Medraj, The impact of microstructure on the permeability of metal foams, 2004 (2004).

[47] F. Streiff, In-line dispersion and mass transfer using static mixing equipment, Sulzer Technical Review (1977).